Soft Matter



PAPER View Article Online



Cite this: DOI: 10.1039/d3sm00224a

Stress and stretching regulate dispersion in viscoelastic porous media flows†

Manish Kumar, D‡a Derek M. Walkama,‡bc Arezoo M. Ardekani Da and Jeffrey S. Guasto D*b

In this work, we study the role of viscoelastic instability in the mechanical dispersion of fluid flow through porous media at high Péclet numbers. Using microfluidic experiments and numerical simulations, we show that viscoelastic instability in flow through a hexagonally ordered (staggered) medium strongly enhances dispersion transverse to the mean flow direction with increasing Weissenberg number (Wi). In contrast, preferential flow paths can quench the elastic instability in disordered media, which has two important consequences for transport: first, the lack of chaotic velocity fluctuations reduces transverse dispersion relative to unstable flows. Second, the amplification of flow along preferential paths with increasing Wi causes strongly-correlated stream-wise flow that enhances longitudinal dispersion. Finally, we illustrate how the observed dispersion phenomena can be understood through the lens of Lagrangian stretching manifolds, which act as advective transport barriers and coincide with high stress regions in these viscoelastic porous media flows.

Received 20th February 2023, Accepted 16th August 2023

DOI: 10.1039/d3sm00224a

rsc.li/soft-matter-journal

1 Introduction

The flow of viscoelastic fluids through porous media governs material transport and mixing in a range of geophysical, biological, and industrial systems. 1,2 Bacterial biofilms proliferate in soils and cause infections in bodily tissue,3 and filtration media are used in food and polymer processing.4 Polymer additives improve the efficacy of hydraulic fracturing and enhanced oil recovery (EOR),5,6 including the remediation of oil ganglia.⁷⁻¹¹ In the latter case of EOR for example, despite extensive efforts to observe and understand the impact of viscoelastic flow, no globally accepted remediation mechanism via polymer additives has been established. 12-15 However, the onset of unsteady velocity fluctuations in such viscoelastic porous media flows16-18 appears to play a critical role in microscale transport, 16,19-21 where porous microstructure couples pore-scale viscoelastic flows²² to sample-scale transport properties.²³ The non-Newtonian rheology of viscoelastic fluids encodes a memory of the flow history, whose nontrivial dependence on pore geometry24-27 can result in

In the absence of inertia, strong elastic stresses cause viscoelastic flow instabilities in porous media, which are heavily dependent on the flow geometry.34,36 The transition to chaotic dynamics in viscoelastic flows is characterized by the Weissenberg number, Wi = $\tau \dot{\gamma}$, which compares elastic forces to viscous forces. Here, τ is the fluid relaxation time and $\dot{\gamma} = U/d$ is the characteristic shear rate, where U is the average flow speed and d is the characteristic obstacle diameter. Chaotic velocity fluctuations at large Wi have been shown to enhance transverse dispersion in ordered porous media flows 16,37 via a "lanechanging" effect.38 In contrast, markedly weaker dispersion enhancement has been reported for viscoelastic flows in disordered media. 19-21 Recent experiments have shed new light on the geometry-dependent transition to chaos and the resulting flow topologies, which ultimately regulate the dispersion properties. The critical Weissenberg number, Wicr, is highly sensitive to both the disorder of the medium³⁴ and orientation of ordered media relative to the flow.³⁶ Preferential flow paths in disordered media and along lattice directions in periodic media reduce extensional deformation and stress and ultimately suppress the transition to chaos compared to staggered obstacle arrangements in ordered systems at the same Wi.34,36 This topological and dynamical shift in the flow field with geometry must be intrinsically linked to the transport properties. However, a comprehensive understanding of how

viscoelastic instability. 16,28-36 A deeper understanding of the interplay between rheology, flow structure, and dispersion is paramount to predicting material transport in viscoelastic porous media flows.

^a Department of Mechanical Engineering, Purdue University, 585 Purdue Mall, West Lafayette, Indiana 47907, USA

b Department of Mechanical Engineering, Tufts University, 200 College Avenue, Medford, Massachusetts 02155, USA. E-mail: Jeffrey.Guasto@tufts.edu

^c Department of Physics and Astronomy, Tufts University, 574 Boston Avenue, Medford. Massachusetts 02155. USA

[†] Electronic supplementary information (ESI) available. See DOI: https://doi.org/10.1039/d3sm00224a

[‡] These authors contributed equally to this work.

Paper Soft Matter

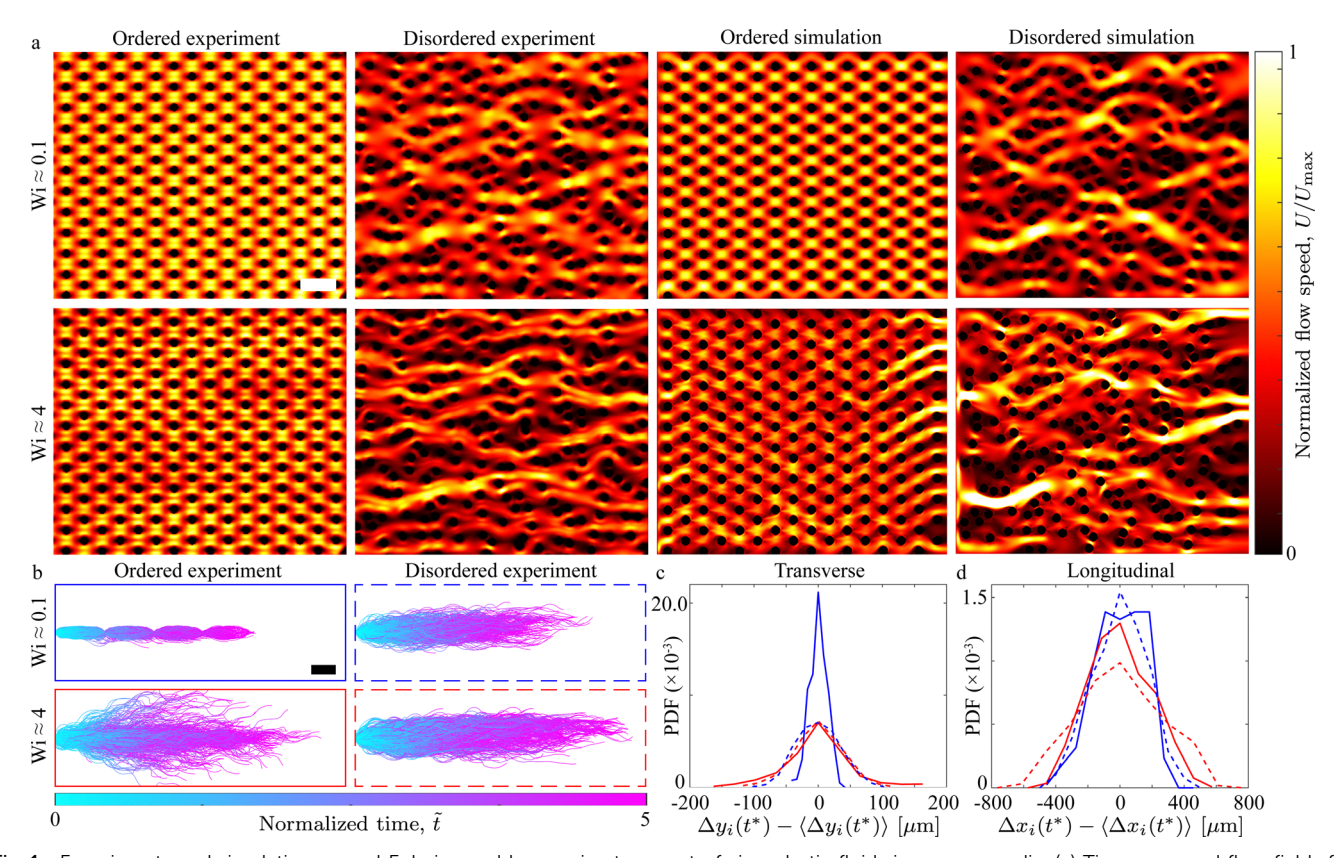


Fig. 1 Experiments and simulations reveal Eulerian and Lagrangian transport of viscoelastic fluids in porous media. (a) Time-averaged flow fields for experiments and respective simulations at various Wi for ordered and disordered porous geometries. Flow is left to right. Scale bar, 120 μ m. (b) Experimentally measured particle trajectories with initial position subtracted, $\Delta \mathbf{x}_i(\tilde{t}) = \mathbf{x}_i(\tilde{t}) - \mathbf{x}_i(0)$, for dimensionless time, $\tilde{t} = tU/l$, in the range $0 \le \tilde{t} \le 5$. Scale bar, 60 μ m. (c) and (d) Transverse and longitudinal relative displacement distributions, respectively, $\Delta \mathbf{x}_i(t^*) - \langle \Delta \mathbf{x}_i(t^*) \rangle$, corresponding to (b) at normalized time, $t^* \equiv \tilde{t} = 5$. Color and line type correspond to panel borders in (b).

viscoelastic flow instabilities regulate dispersion in porous media remains lacking.

In this work, we characterize how changes in the topology (i.e., structure) of viscoelastic flows regulate anisotropic dispersion in porous media, and we elucidate the underlying mechanisms for geometry-dependent transport. Microfluidic experiments are complemented by numerical simulations for quasi-two-dimensional model porous media for both hexagonally ordered (staggered) and disordered arrays of cylindrical pillars. Our results capture the accepted enhancement of transverse dispersion via flow instability in ordered flow and also reveal that the amplification of preferential flow paths in the disordered media increases longitudinal dispersion [Fig. 1]. Furthermore, recent theoretical work based on a Lagrangian analysis of viscoelastic flows demonstrated that the fluid stretching field closely reflects the polymeric stress topology.³⁹ We show that transverse and longitudinal dispersion can be understood through the structure of the Lagrangian stretching field, whose manifolds act as barriers to advection and dynamically guide transport in both steady and unsteady flows. These results demonstrate a potential mechanism for tuning anisotropic dispersion, and they illustrate a direct link between elastic stress and transport in viscoelastic porous media flows.

2 Methods

2.1 Experimental methods

Following established approaches from previous work,34 microfluidic devices were designed and fabricated with 25 mm long, 4 mm wide, and 50 μm high straight main channels, which contain arrays of cylindrical pillars (diameter, $d = 50 \mu m$) in both an ordered and a disordered configuration. Photolithography masks were generated by first specifying an ordered, hexagonal array in a staggered orientation relative to the flow direction (ESI,† Fig. S1),³⁶ which had a lattice constant, a =120 µm. The disordered geometry was created by randomly perturbing the pillar locations from the original lattice within a hexagonal circumradius of a (ESI,† Fig. S1). The porosity of both the ordered and disordered geometries is ≈ 0.84 . The viscoelastic fluid is a solution of high molecular weight polyacrylamide (PAA; 18×10^6 MW) at a concentration of 150 ppm of PAA in a viscous Newtonian solvent (97% aqueous glycerol).40 The solution was prepared by mixing 1 g of PAA into 200 mL of DI water using a magnetic stirrer for 1 h. 3 g of the aqueous PAA solution was mixed with 97 g of glycerol for 12 h. Finally, the fluid was seeded with 0.5 μm (F8813 FluoroSpheres, Life Technologies) and 1 µm (F13081 Fluoro-Spheres, Life Technologies) diameter tracer particles for

simultaneous particle image velocimetry (PIV) and particle tracking, respectively.

Capillary breakup extensional rheology (CaBER) was used to characterize the (longest) relaxation time, τ , of the PAA solutions [ESI,† Fig. S2(a)],41 which provides a more relevant measure of the relaxation time for strongly elongational flows compared to shear rheology. 42,43 The PAA solution was stretched between the ends of two circular cylinders, and the measured exponential decay rate of the liquid bridge diameter (3τ) gave a relaxation time $\tau = 1.14 \pm 0.1$ s (N = 6). The shear-rate dependence of the viscoelastic fluid was characterized using a strain controlled rheometer (TA-2000) with a cone and plate geometry [ESI,† Fig. S2(b)]. The polymer solution was presheared at a rate of 1 s⁻¹ for 120 s, then each measurement was held at the respective shear rate for 60 s and measured for 15 s. The PAA solution exhibited a weak shear thinning behavior, which is well fitted by the Carreau-Yasuda model.⁴⁴ The measured shear viscosity, η , was in the range 2 Pa s $\geq \eta \geq$ 0.5 Pa s for shear rates in the range $0.01 \le \dot{\gamma} \le 10 \text{ s}^{-1}$.

The viscoelastic flow was driven by a pressure controller (Elveflow OB1) through the microfluidic pillar array channel. Epifluorescence video microscopy (Nikon Ti-e; 10x, 0.3 NA objective) captured the motion (100 fps; Andor Zyla) of fluorescent tracer particles at the mid-depth of the channel. Timeresolved velocity fields, $\mathbf{u}(\mathbf{x},t)$, were measured using PIV, ⁴⁵ and Lagrangian statistics were obtained by simultaneous particle tracking. For the viscoelastic fluid and imaging system used here, a maximum Wi of Wi < 5 was found to provide reliable imaging for PIV. These conditions corresponded to a maximum Reynolds number of Re = $\rho Ud/\eta_0 \lesssim 10^{-4}$ (density, ρ ; mean flow speed, U; zero shear viscosity, η_0 ; see also ESI†), which ensured that inertial effects were negligible and that the emergence of flow instability only depended on elastic effects. The Péclet numbers, Pe = $Ud/D(\eta)$, for the experiments were in the range $10^5 \le \text{Pe} \le 10^9$, where D accounts for the viscosity dependent Stokes-Einstein diffusion coefficient of the tracers. These large Pe suggest that transport in experiments was advection dominated, and thus, we assume that tracer diffusion has negligible impact on measured dispersion.

2.2 Numerical methods

The numerical simulations were performed in a twodimensional domain that was designed to exactly match the region-of-interest in experiments [Fig. 1(a) and ESI,† Fig. S1] via computer-generated photomasks. The flow of incompressible polymeric fluid in the interstitial region of the porous geometry is described by the conservation of mass and momentum as:

$$\nabla \cdot \mathbf{u} = 0, \tag{1}$$

$$\rho \left(\frac{\partial \mathbf{u}}{\partial t} + \mathbf{u} \cdot \nabla \mathbf{u} \right) = -\nabla p + \nabla \cdot \boldsymbol{\sigma}, \tag{2}$$

where \mathbf{u} and p are the fluid velocity and pressure fields, respectively. The total stress tensor σ is written as $\sigma = \sigma_s + \sigma_p$, where σ_s and σ_p are the solvent and polymeric stress tensor, respectively. For the Newtonian solvent, σ_s is given as $\sigma_s = \eta_s(\nabla \mathbf{u} + \nabla \mathbf{u}^T)$, where η_s is the solvent viscosity. We chose the FENE-P constitutive equation to calculate the polymeric stresses because it captures both elasticity and shear thinning behaviours as well as finite extensibility of polymeric

$$\boldsymbol{\sigma}_{p} + \frac{\tau}{f} \stackrel{\nabla}{\boldsymbol{\sigma}}_{p} = \frac{b\eta_{p}}{f} (\nabla \mathbf{u} + \nabla \mathbf{u}^{T}) - \frac{D}{Dt} (\frac{1}{f}) [\tau \boldsymbol{\sigma}_{p} + b\eta_{p} \mathbf{I}], \quad (3)$$

where η_p is the polymeric contribution to the zero shear viscosity of the solution, $\eta_0 = \eta_s + \eta_p$. I is the identity tensor and D/Dt is the material derivative. The function f is described as:

$$f(\boldsymbol{\sigma}_{\mathrm{p}}) = \frac{L^2 + \frac{\tau}{b\eta_{\mathrm{p}}} \mathrm{tr}(\boldsymbol{\sigma}_{\mathrm{p}})}{L^2 - 3},\tag{4}$$

where $b = L^2/(L^2 - 3)$, and the parameter $L^2 = 3R_0^2/R_e^2$ represents the ratio of the maximum allowable length, R_0 , to the equilibrium length, R_e , of the polymeric chains. 46-48 For the FENE-P model, a typical range of L^2 is 10–1000, 21,47,49,50 which reduces to the Oldroyd-B constitutive model in the limit of $L^2 \to \infty$. The upper convective time derivative operator ∇ used in eqn (3) is given by:

$$\overset{\nabla}{\boldsymbol{\sigma}}_{p} = \frac{D\boldsymbol{\sigma}_{p}}{Dt} - \boldsymbol{\sigma}_{p} \cdot \nabla \mathbf{u} - \nabla \mathbf{u}^{T} \cdot \boldsymbol{\sigma}_{p}. \tag{5}$$

The numerical simulations were performed using the opensource framework RheoTool⁵¹ integrated with OpenFOAM,⁵² where the equations were discretized using a finite volume method and the log-conformation approach was used to calculate the polymeric stress tensor.^{53,54} The relationship between the polymeric stress tensor, σ_p , and the log-conformation tensor, Θ , is given as:

$$\boldsymbol{\sigma}_{\mathrm{p}} = \frac{\eta_{\mathrm{p}}}{\tau} (f e^{\mathbf{\Theta}} - b \mathbf{I}). \tag{6}$$

The implementation and the validation of the numerical tool can be found in previous works (ESI,† Fig. S3).51,55 Viscoelastic models often fail to represent the polymeric fluids used in the industry, especially at high deformation rates, 1,43,56 and there are studies in the literature where the model parameters have been adjusted to match the experimental observations even for simpler setups. 49,57,58 Therefore, we focus on a qualitative comparison between experiments and simulations in the present study. The dimensionless numbers used in the simulations were: Re = 10^{-4} , $0.1 \le \text{Wi} \le 5$, $\beta = \eta_s/(\eta_s + \eta_p) = 0.02$, and L^2 = 1000. The flow was driven with a constant inlet velocity of 50 μm s⁻¹ on the left side of the channel with no-slip boundaries on the top and bottom walls, and fully developed boundary conditions (i.e., zero-gradient) at the outlet [Fig. 1]. While the choice to use 2D simulations versus 3D was driven by the high computational cost, 2D simulations were found to capture all of the essential features of these viscoelastic flows [Fig. 1]. In the present study, elastic effects completely dominate over inertial effects as the elasticity number (El), which measures the relative importance of elastic and inertial forces, is El \sim $O(10^4) \gg 1$. Therefore, the Weissenberg number in the

simulation has been altered by changing the relaxation time

 $(\tau = 0.1-5 \text{ s}).$ For both experiments and simulations, the Lagrangian stretching, $S(\mathbf{x},t)$, is determined from the time resolved flow field^{59,60} by using established methods.^{39,61,62} Briefly, fluid element positions, x_0 , at time $t = t_0$ are deformed by a flow field, $\mathbf{u}(\mathbf{x},t)$, and advected to new positions, \mathbf{x} , at time, $t_1 = t_0 + \lambda$. The flow map, $\mathbf{F}_{\lambda}(\mathbf{x}_0) = \mathbf{x}$, is determined as the solution to $\frac{d\mathbf{x}}{dt} = \mathbf{u}(\mathbf{x}, t)$, and the (right) Cauchy–Green strain tensor is formed as $\mathbf{C}_{\lambda}^{(\mathbf{R})} = \nabla \mathbf{F}_{\lambda}^{\mathrm{T}} \nabla \mathbf{F}_{\lambda}$. Finally, the stretching field $S(\mathbf{x},t)$ is calculated as the square root of the largest eigenvalue of $C_{\lambda}^{(R)}$, where the corresponding eigenvector gives the principal stretching direction. For all flows, the stretching history is determined by backward time integration, and the integration time was chosen as the fluid relaxation time $(\lambda = -\tau)^{39}$ F₂ was found through numerical integration (ODE45, MATLAB) for initial positions on a regular grid (251 \times 351) along with four auxiliary points each (1 μ m separation). $\nabla \mathbf{F}_{\lambda}$ was computed through central differences of the auxiliary points, and

3 Results

Paper

3.1 Anisotropic Lagrangian transport in porous media

MATLAB was used for the stretching field calculations.

The stability analysis of viscoelastic flows through the geometries considered in the present study has been performed in Walkama et al.,³⁴ where the temporal fluctuation of the flow speed was used to characterize the stability. Flow through hexagonally ordered (staggered) geometries in both experiments and simulations exhibit a transition to unstable flow at a critical Weissenberg number, $Wi_{cr} \approx 0.5.^{34}$ However, the time-averaged flow fields do not show a strong topological change with Wi due to the high degree of geometric symmetry [Fig. 1(a)]. In contrast, disordered geometries stabilize these flows via the formation of preferential flow paths, 63 where extensional fluid deformations - and consequently polymer stretching – are reduced. 34,36 Time-averaged flow fields through disordered media in both experiments and simulations display a topological shift from a Newtonian flow [Fig. 1(a)], where filaments form as Wi is increased and the flow field becomes more heterogeneous. As in previous works, 34,36 this Eulerian picture points to a trade-off between stability and channelization that is mediated by pore microstructure. However, to gain deeper insight into the effect of geometry on particle dispersion in viscoelastic flows, we adopt a Lagrangian description of transport.

Lagrangian analysis of fluid transport reveals that lateral and longitudinal tracer displacements are enhanced at high Wi for the ordered and disordered porous geometries, respectively. Particle tracking provides tracer particle trajectories in time, $\mathbf{x}_i(\hat{t})$, where i represents an individual particle track. The normalized time, $\tilde{t} = tU/l$, corresponds to the number of pores traveled for a given characteristic (mean) flow speed, U, and stream-wise pore spacing, $l = a \sin 60^\circ$. Examination of the net displacement of the fluid tracers with respect to their initial

positions, $\Delta \mathbf{x}_i(\hat{t}) = \mathbf{x}_i(\hat{t}) - \mathbf{x}_i(0)$, demonstrates how geometry influences transport through viscoelasticity [Fig. 1(b)]. Tracers in the ordered geometry at small Wi tamely oscillate back and forth, as they weave through the pillar array following streamlines in the steady flow. Conversely, at Wi = 4 > Wi_{cr}, tracers exhibit wild lateral excursions accompanied by a moderate enhancement of longitudinal displacement. The former is consistent with previous observations of "lane-changing", ¹⁶ which is a consequence of temporal velocity field fluctuations. ³⁴ In the disordered geometry, tracers laterally explore a relatively large swatch of the porous channel by virtue of the meandering streamlines at low Wi, with little change at higher Wi [Fig. 1(b)]. While the disordered flow remains steady at Wi = 4 (see also Fig. 3 in ³⁴), tracer displacements are appreciably enhanced in the longitudinal direction.

The displacement distributions relative to the mean, $\Delta \mathbf{x}_i(t^*) - \langle \Delta \mathbf{x}_i(t^*) \rangle$, at a fixed time $(t^* \equiv \tilde{t} = 5)$ more clearly show the anisotropic enhancement of tracer excursions in both the ordered and disordered systems at high Wi [Fig. 1(c) and (d)]. Here, $\langle \cdot \rangle$ indicates an ensemble average. The transverse displacement [Fig. 1(c)] exhibits a narrow distribution for low Wi in the ordered media (blue solid) due to the high Péclet number, stable flow. At high Wi, the ordered media shows large displacements in the transverse direction (red solid), consistent with the onset of the elastic instability. Transverse disordered flow, on the other hand, is generally unaffected by increasing Wi and shows little to no change (blue and red dashed for low and high Wi, respectively). Surprisingly, longitudinal displacements [Fig. 1(d)] show the opposite effect as a function of disorder. Longitudinal displacements in the ordered system (solid curves) show little change with Wi. However, the disordered media exhibits a broader tracer displacement distribution for high Wi (dashed red) compared to low Wi (dashed blue). Thus, tracers disperse by traveling both significantly faster and slower than the mean flow speed in disordered media at high Wi.

3.2 Mean squared displacement analysis reveals dispersive spreading of fluid tracers

The variance of the displacement distributions [Fig. 1(c) and (d)] defines the advection-free mean squared displacement (MSD) at time, \tilde{t} , which indicate the nature and rate of spreading of the tracer ensemble:

$$\sigma_{\rm T}^{2}(\tilde{t}) = \langle (\Delta y_{i}(\tilde{t}) - \langle \Delta y_{i}(\tilde{t}) \rangle)^{2} \rangle, \tag{7}$$

$$\sigma_{\rm L}^{2}(\tilde{t}) = \langle (\Delta x_{i}(\tilde{t}) - \langle \Delta x_{i}(\tilde{t}) \rangle)^{2} \rangle. \tag{8}$$

The MSD describes the average separation of fluid parcels from one another in time due to both the mechanical dispersion and flow instability in the transverse (σ_T^2) and longitudinal (σ_L^2) directions, respectively. The transverse MSD in the ordered media exhibits oscillations at low Wi reflective of the obstacle periodicity, but the MSD saturates due to the sampling of streamlines with finite amplitude displacements from the mean flow direction. As Wi increases and the flow becomes elastically unstable [Fig. 2(a), solid curves], the displacements

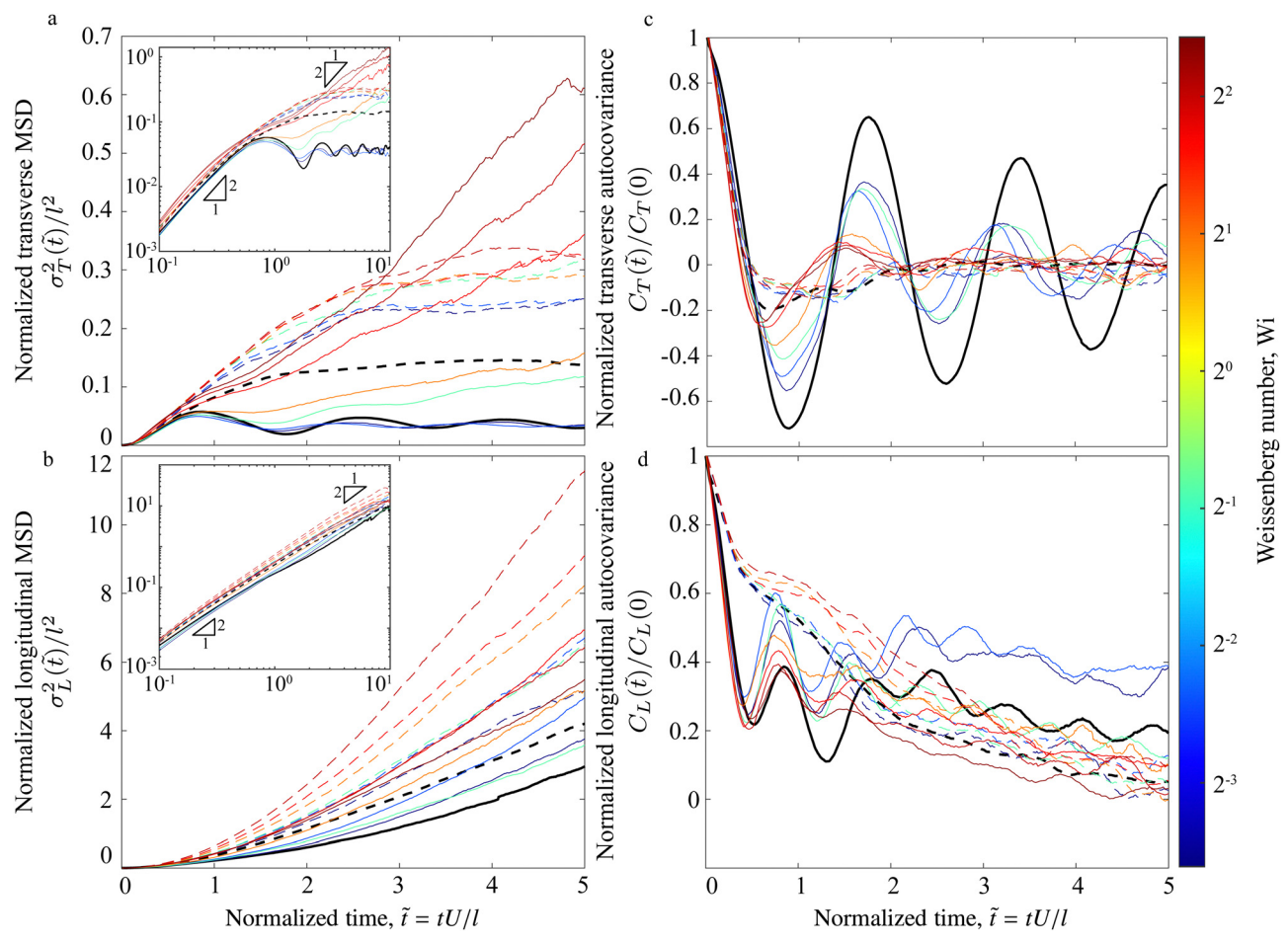


Fig. 2 Experimental Lagrangian flow statistics inform the effect of geometry on tracer dispersal. (a) and (b) Normalized transverse and longitudinal mean squared displacement, respectively, as a function of normalized time for ordered (solid) and disordered (dashed) media at various Wi. Insets show the same data on a log-log scale. (c) and (d) Normalized transverse and longitudinal autocovariance, respectively, as a function of normalized time for ordered (solid) and disordered (dashed) flow at various Wi numbers. Black curves correspond to Newtonian fluid flow (100% glycerol) at comparable low Re and high Pe numbers for all plots.

at long times are unbounded and grow superlinearly in time [Fig. 2(a), inset], which is indicative of superdiffusive transport (i.e., MSD $\propto t^{\alpha}$ with $1 < \alpha < 2$). However, in the disordered geometry, all transverse MSDs plateau after $\approx 2-3$ pore lengths and are only mildly affected by Wi [Fig. 2(a), dashed curves]. While all transverse MSDs are ballistic at short times ($\alpha \approx 2$) [Fig. 2(a), inset], only MSDs for the transverse, high Wi ordered flow continue growing superlinearly at long times due to the elastic instability. Mechanical dispersion in the flow direction^{64,65} causes longitudinal MSDs to be unbounded. While all longitudinal MSDs are superdiffusive [Fig. 2(b), inset], MSDs for viscoelastic flows grow faster in the disordered media [Fig. 2(b), dashed curves] compared to ordered media [Fig. 2(b), solid curves], relative to their respective Newtonian flows.

Dispersion tensor for viscoelastic porous media flow

Due to the anisotropic spreading of the tracer ensemble in the transverse and longitudinal flow directions⁶⁶ [Fig. 1(b) and (c)], the transport is parameterized by the dispersion tensor, $D_{T,L}$.

Furthermore, superdiffusive transport [Fig. 2(a) and (b)] stemming from mechanical dispersion in this high Pe regime suggests that dispersion coefficients may vary indefinitely in time, and thus we examine the time-dependent dispersion tensor:20,67

$$D_{\mathrm{T,L}}(\tilde{t}) = \int_0^{\tilde{t}} C_{\mathrm{T,L}}(t') \mathrm{d}t'. \tag{9}$$

Here, $C_{\text{T,L}}(\tilde{t})$ is the time-dependent velocity autocovariance that quantifies the temporal correlation of tracer velocity:

$$C_{\mathrm{T}}(\tilde{t}) = \frac{1}{N} \sum_{i=1}^{N} \left(u_{yi}(\tilde{t}) - \left\langle u_{yi}(\tilde{t}) \right\rangle \right) \left(u_{yi}(0) - \left\langle u_{yi}(0) \right\rangle \right), \quad (10)$$

$$C_{L}(\tilde{t}) = \frac{1}{N} \sum_{i=1}^{N} \left(u_{xi}(\tilde{t}) - \langle u_{xi}(\tilde{t}) \rangle \right) (u_{xi}(0) - \langle u_{xi}(0) \rangle), \tag{11}$$

where the $u_{vi}(\tilde{t})$ and $u_{xi}(\tilde{t})$ are respectively the transverse and longitudinal velocity components of particle i, and $\langle \cdot \rangle$ is an ensemble average over N particles. The transverse **Paper** Soft Matter

autocovariance is periodic about zero in the ordered geometry, but the oscillations lose coherence with the onset of the instability as Wi increases. However, as the instability drives lane changing, transverse particle velocities gain a slight net correlation due to the motion over one or more pores lateral to the flow. For disordered flow, $C_{\rm T}$ rapidly decays and appears to have little dependence on Wi [Fig. 2(c)], due to the random uncorrelated flow paths through the medium. Similar to the transverse direction, the longitudinal autocovariance for ordered flow exhibits periodic peaks that lose coherence as Wi increases [Fig. 2(d)], due to the onset of spatiotemporal velocity fluctuations. Conversely, C_L for disordered flow shows an increase in the correlation time beyond a Newtonian fluid as Wi is increased. This increased velocity correlation stems from the formation of preferential flow paths that transport fluid in the longitudinal direction,³⁴ which we expect to lead to increased dispersion.

The time-dependent dispersion tensor serves as a primary measure of augmented anisotropic transport. Dispersion coefficients (especially longitudinal) naturally increase with mean

flow speed. Therefore, to infer the explicit effect of fluid elasticity, the time-dependent dispersion coefficients were normalized with the maximum value of dispersion coefficients obtained for a Newtonian fluid for the same mean flow speed. In these high Péclet flows, transverse dispersion coefficients in both experiments [Fig. 3(a)] and simulations [Fig. 3(b)] either oscillate about zero (ordered) or decay to zero (disordered) for stable flows (Wi \leq Wi_{cr}). In experiments, the instability only occurs in the ordered flow [Fig. 3(a), solid curves]. However, in simulations, some velocity fluctuations in both ordered and disordered flows cause finite values of D_T at long times and high Wi [Fig. 3(b)]. While both geometries ultimately become unstable in simulations, this effect is more pronounced in high Wi ordered flows, indicated by elevated long-time dispersion [Fig. 3(b)] compared to the disordered flow. In the longitudinal direction, D_L grows approximately linearly for ordered flow at low Wi, but plateaus at high Wi [Fig. 3(c), solid curves], indicating an effectively diffusive regime. The linear growth is due to the constant, non-zero autocovariance in steady flows through the ordered geometry. Once the flow becomes unstable

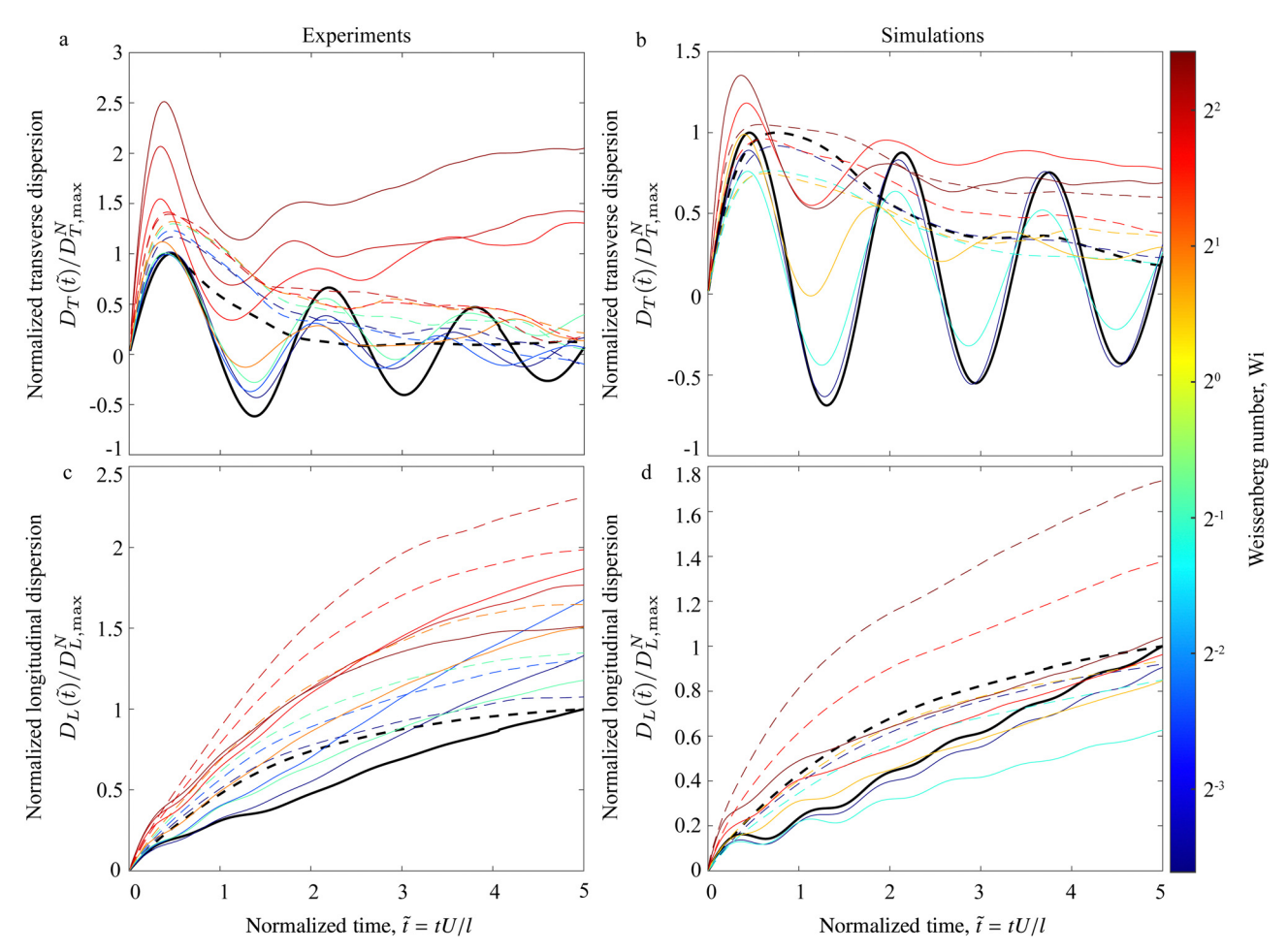


Fig. 3 Comparison of dispersion tensor components for experiments and simulations in ordered (solid) and disordered (dashed) media. (a) and (b) Transverse dispersion coefficients for experiments and simulations, respectively. (c) and (d) Longitudinal dispersion coefficients for experiments and simulations, respectively. Black curves correspond to Newtonian fluid flow (100% glycerol) at comparable low Re and high Pe numbers for all plots. Values for all dispersion coefficients are normalized by their respective maximal Newtonian values for ordered and disordered media in the longitudinal and transverse direction across experiments and simulations (see also ESI,† Fig. S4).

in experiments (Wi \gtrsim Wi_{cr}), dispersion values increase at small times but plateau at long times [Fig. 3(c), solid curves] due to decorrelation observed in C_L [Fig. 2(d), solid curves]. This effect is also seen in simulations [Fig. 3(d), solid curves], but the dispersion coefficient does not reach a constant value in time. In simulations, we observe far less diagonal flow due to the reduced system size compared to experiments. As a result of this correlated longitudinal motion, D_{τ} does not reach a steady state in simulations. Due to the limited domain size and ability to track particles over very large distances in experiments, it is unclear when dispersion in high Wi disordered flow reaches a steady state [Fig. 3(c), dashed curves]. However, the magnitude of dispersion is larger than ordered flows at all times for high Wi. This observation also holds true for simulations [Fig. 3(d), dashed curves], where D_L for disordered media is much larger than for ordered media and is still growing for long times. Furthermore, in ordered geometries aligned along the flow direction, ³⁶ we speculate that such highly stable, unidirectional flows will lead to faster growth of D_L compared to the disordered geometry due to Taylor-like dispersion,68 but this hypothesis remains to be tested.

We have systematically quantified the transport properties and stability of viscoelastic flows through porous media. These results show that there is a clear trade-off between rheologyenhanced transport and geometry that also accompanies the stabilizing effect of preferential flow paths in the disordered media. These viscoelastic fluids are composed of elastic polymers suspended in a carrier fluid, which stretch dramatically in extensional strain compared to shear strain. 69,70 Polymer elasticity embeds a memory into the fluid, whereby polymers continue to stretch and accumulate stress as they move through both space and time via advection. Flow through the staggered ordered media becomes chaotic due to extensional stresses at high Wi, whereas preferential flow paths can alleviate extension and promote stability in the disordered media. 34,36 The topology of the polymeric stress field has been known to regulate flow states in viscoelastic flows. 24,26,27,71 Polymeric stress is thus integral to both enhanced transport and elastic stability in these systems, but access to the polymeric stress field in experiments is challenging.⁷² Recently, a Lagrangian analysis of fluid deformation was demonstrated to provide direct insight into the topology of the polymeric stress field from readily measurable flow field data, 39 which is a key to the comprehensive understanding of the transport in these systems.

3.4 Lagrangian stretching guides fluid flow

Lagrangian coherent structures (LCS)⁵⁹ characterize material lines that organize fluid transport, which have been applied broadly across scales to understand ocean flow patterns, chaotic mixing, 60 bacterial transport, 62 and complex fluid flows. 39 Key to LCS analysis is the concept of the Lagrangian fluid stretching field, which quantifies the extensional strain history of fluid elements and is closely linked to the finite-time Lyapunov exponent (FTLE) field. Manifolds of the stretching field are curves that correspond to ridges in the stretching field

having a locally large value of S [Fig. 4(b)]. 59 Such manifolds act as barriers to advective transport, and recently, were shown to be highly correlated with the topology of the polymeric stress field in viscoelastic flows.³⁹ Thus, the Lagrangian stretching potentially provides a direct link to understand how polymer stress regulates dispersive transport in viscoelastic porous media flows.

Lagrangian stretching fields, $S(\mathbf{x},t)$, were calculated directly from both the experimentally measured and simulated velocity fields (see Methods). 39,59,61,62 The viscoelastic fluid relaxation time, τ , was chosen as a natural integration time over which the stretching history was computed for all Wi. Stretching fields for both the ordered and disordered media [Fig. 4(a)] reveal sharp regions of high stretching (manifolds) that generally emanate from the hyperbolic flow regions on the downstream sides of the pillars, including in unsteady flow conditions [Fig. 4(e)]. Striations in S observed downstream of pillars in experiments are likely due to finite PIV resolution.⁷³ Importantly, simulations also provide the time-dependent stress tensor, $\sigma(\mathbf{x},t)$, and enable direct comparison with the Lagrangian stretching [Fig. 4(b)]. In line with recent work, ³⁹ the trace of the polymeric stress tensor [Fig. 4(b)] mirrors the topology of the stretching manifolds [Fig. 4(a)] for both ordered and disordered flow simulations. To quantify the correlation between the topologies of stress and stretching fields, the cross-correlation is defined

$$\Phi(\delta \mathbf{x}) = \frac{\left[\operatorname{tr}(\boldsymbol{\sigma}(\mathbf{x} + \delta \mathbf{x})) - \langle \operatorname{tr}(\boldsymbol{\sigma}) \rangle\right] \cdot \left[S(\mathbf{x}) - \langle S \rangle\right]}{\langle \operatorname{tr}(\boldsymbol{\sigma}) \rangle \langle S \rangle},$$

where $\langle \cdot \rangle$ denotes the mean value over all **x**, and δ **x** is the shifted position. Large values of Φ indicate large values for both $tr(\sigma)$ and S. The strongest correlation occurs for $\delta x = 0$ due to the overlap of the filamentous stretching and stress fields [Fig. 4(c)], which is indicated by the elongated features of Φ for the ordered media in the longitudinal direction. Examining the magnitude of the cross-correlation in the flow direction (δx) shows that the strength of Φ initially increases with Wi before diminishing at larger Wi [Fig. 4(d)], likely due to the onset of strong temporal fluctuations.

The concordance between Lagrangian stretching and stress demonstrated by simulations provides insight into the role of stress in dispersive transport for viscoelastic flow experiments in porous media.³⁹ In experiments for ordered media, enhanced transverse dispersion is driven by elastic instability. The accompanying mobility of stretching manifolds [Fig. 4(e)] – which act as barriers to advective transport - effectively guide the local flow. A time series of stretching fields from ordered experiments at high Wi shows that stretching manifolds span the pillar array in the longitudinal direction. Their lateral fluctuations in the transverse direction illustrate the mechanism of lane-changing¹⁶ in enhanced transverse dispersion. Conversely, stable flows in disordered media at high Wi disallow transverse material flux. In this case, stretching manifolds elongate as Wi increases and cut off regions of locally high pillar density resulting in the formation of stagnation (dead) zones [Fig. 4(a)].³⁷ However, the stretching manifolds in

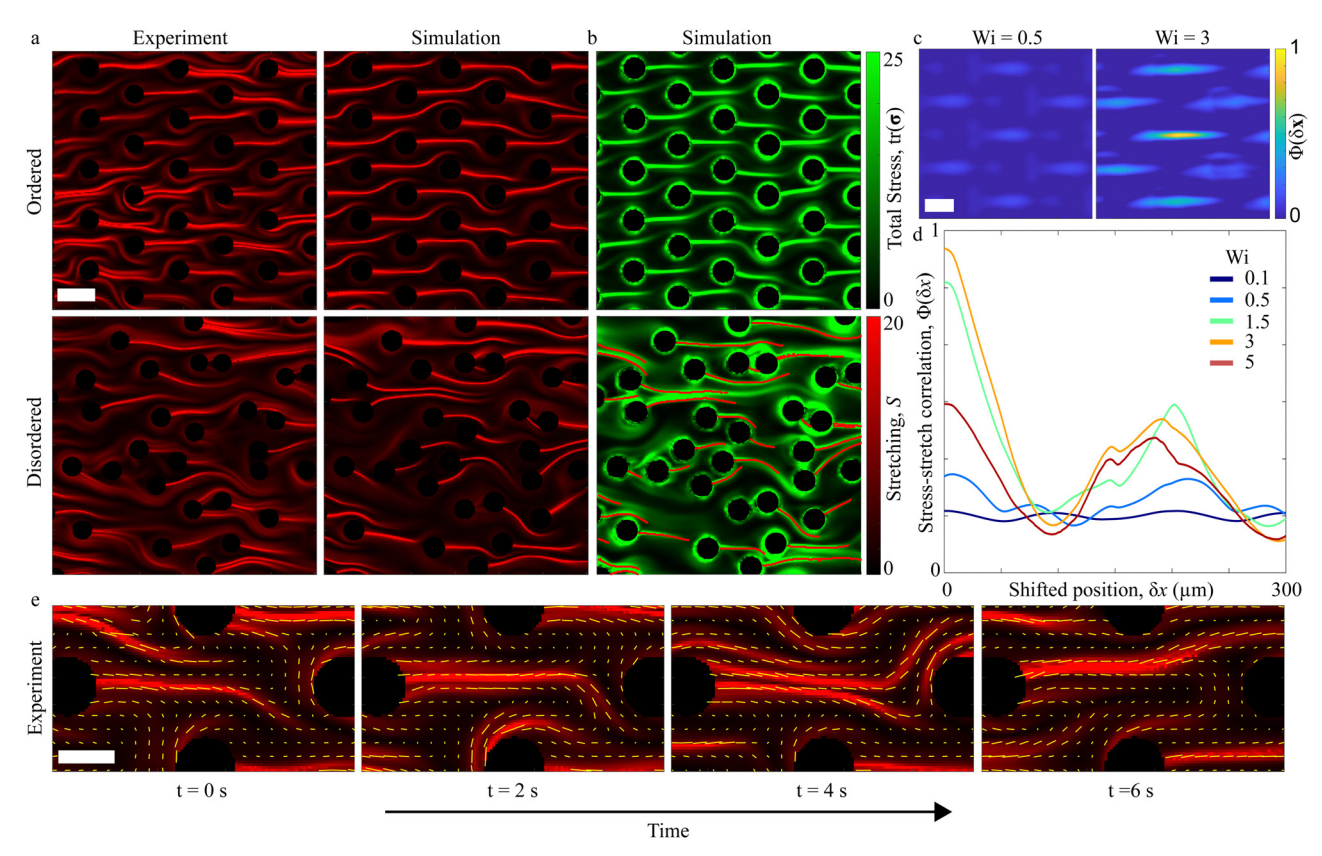


Fig. 4 Lagrangian stretching correlates to stress and illustrates the pathways guiding fluid transport. (a) Stretching fields for both the ordered and disordered geometries in experiments and simulations at Wi = 3. Scale bar, 100 µm. (b) Stress fields from simulations for corresponding flows in panel (a). Magenta lines show manifolds of the stretching field, which correspond to ridges of maximal local stretching. (c) Stress-stretch correlation maps for simulated, ordered flow fields at Wi = 0.5 (left) and Wi = 3 (right). Center corresponds to $\delta x = 0$. Scale bar, 50 µm. (d) Stress-stretch correlation for different shift positions in the longitudinal (x) direction for simulated flow fields at various Wi ($\delta y = 0$). (e) Time series of experimental stretching fields showing a wavering stretching manifold in ordered porous media at Wi = 3. Vector fields indicate the principle stretching direction. Scale bar, 50 µm.

the regions of low pillar density facilitate longitudinal transport by acting as a conduit through the porous media. Thus, the particles trapped in the dead zones travel slower than the mean flow speed, whereas those in conduits travel faster than the mean flow speed, leading to the enhanced heterogeneity of spatial flow speed [Fig. 1(d)]. In sum, instability in ordered media allows stretching manifolds to mobilize, whereas the stability in disordered media forces the stretching manifolds, and therefore the stress, to cut off regions of flow that were previously available at low Wi.

Efforts have been made to investigate viscoelastic instabilities in 3D ordered and disordered porous geometries. 35,74 Similar to the 2D ordered geometry, viscoelastic flow through 3D ordered geometry becomes unstable at high Wi.74 For viscoelastic flow through 3D disordered porous media,³⁵ the elevated disorder and pore connections are expected to enhance transport and mixing. The investigation of the formation of dead zones and their effect on longitudinal dispersion in 3D geometries would provide useful insight for field applications such as EOR and groundwater remediation.^{6,75} The Lagrangian stretching concept which has been used here as a proxy of polymeric stress field measurement can be extended to 3D geometry, where the stretching manifolds will

be characterized by the surfaces⁵⁹ instead of the strands. This approach could be used to understand particle transport in 3D porous geometries, but it awaits further exploration.

4 Conclusions

In this work, we quantify dispersion in viscoelastic flow through porous media and show how it is driven by viscoelastic instabilities. Flow through hexagonally-ordered (staggered) porous media enhances transverse dispersion, which is especially prevalent at high Weissenberg numbers. Through a novel Lagrangian analysis of fluid stretching fields, we illustrate that this phenomenon is regulated by stretching manifolds that act as barriers to advective transport and characterize high-stress regions of the flow. At low Wi, material lines are symmetric, stable, and situated between obstacles parallel to flow, while at high Wi, strong lateral fluctuations guide lateral dispersion. Conversely, high Wi flows in disordered porous media remain stable, as previously shown, due to the reduction of extension and the availability of preferential flow paths. 34,36 This flow stability is reflected in stable stretching manifolds that disallow random transverse flows. Stretching manifolds also enhance

spatial flow speed heterogeneity by cordoning off slow flow regions as the stretching manifolds elongate with increasing Wi. This feature results in dead zones between high-speed filaments, where flow is carried longitudinally at disparate respective rates. Thus, these results show that a Lagrangian examination of fluid stretching is essential to gain insight into the coupling between fluid transport and stress through mechanical fluid instability in viscoelastic porous media flows.

Author contributions

All authors conceived the research, interpreted the results, analyzed the data, and wrote the paper. D. M. W. performed experiments. M. K. performed numerical simulations.

Conflicts of interest

There are no conflicts to declare.

Acknowledgements

The authors acknowledge support for this work by National Science Foundation awards CBET-2141349, CBET- 1701392, and CAREER-1554095 (to J. S. G.), and CBET-1700961, CBET-1705371, and CBET-2141404 (to A. M. A.).

Notes and references

- 1 M. Kumar, J. S. Guasto and A. M. Ardekani, *J. Rheol.*, 2022, **66**, 375–397.
- 2 S. S. Datta, A. M. Ardekani, P. E. Arratia, A. N. Beris, I. Bischofberger, G. H. McKinley, J. G. Eggers, J. E. López-Aguilar, S. M. Fielding, A. Frishman, M. D. Graham, J. S. Guasto, S. J. Haward, A. Q. Shen, S. Hormozi, A. Morozov, R. J. Poole, V. Shankar, E. S. G. Shaqfeh, H. Stark, V. Steinberg, G. Subramanian and H. A. Stone, *Phys. Rev. Fluids*, 2022, 7, 080701.
- 3 L. Hall-Stoodley, J. W. Costerton and P. Stoodley, *Nat. Rev. Microbiol.*, 2004, 2, 95–108.
- 4 M. Anguiano and F. J. Suárez-Grau, Z. Angew. Math. Phys., 2017, 68, 45.
- 5 M. Delshad, D. H. Kim, O. A. Magbagbeola, C. Huh, G. A. Pope and F. Tarahhom, *Proc. SPE Symp. Improved Oil Recovery*, 2008, **2**, 1051–1065.
- 6 K. S. Sorbie, *Polymer-improved oil recovery*, Springer Science & Business Media, 2013.
- 7 S. Rodriguez, C. Romero, M. Sargenti, A. Müller, A. Sáez and J. Odell, *J. Non-Newtonian Fluid Mech.*, 1993, **49**, 63–85.
- 8 S. De, P. Krishnan, J. van der Schaaf, J. Kuipers, E. Peters and J. Padding, J. Colloid Interface Sci., 2018, 510, 262–271.
- 9 N. Zamani, I. Bondino, R. Kaufmann and A. Skauge, *J. Pet. Sci. Eng.*, 2015, **133**, 483–495.
- 10 E. Aliabadian, S. Sadeghi, A. Rezvani Moghaddam, B. Maini, Z. Chen and U. Sundararaj, *Fuel*, 2020, **265**, 116918.

- 11 S. Aramideh, P. P. Vlachos and A. M. Ardekani, *Transp. Porous Media*, 2019, **126**, 455–474.
- 12 J. C. Fan, F. C. Wang, J. Chen, Y. B. Zhu, D. T. Lu, H. Liu and H. A. Wu, *R. Soc. Open Sci.*, 2018, 5, 180076.
- 13 B. Wei, L. Romero-Zerón and D. Rodrigue, *J. Pet. Explor. Prod. Technol.*, 2014, 4, 113–121.
- 14 S. J. Haward and J. A. Odell, Rheol. Acta, 2003, 42, 516-526.
- 15 A. Zaitoun, H. Bertin and D. Lasseux, *Proc. SPE Symp. Improved Oil Recovery*, 1998, 1, 285–292.
- 16 C. Scholz, F. Wirner, J. R. Gomez-Solano and C. Bechinger, *Europhys. Lett.*, 2014, **107**, 54003.
- 17 A. Clarke, A. M. Howe, J. Mitchell, J. Staniland, L. Hawkes and K. Leeper, *Soft Matter*, 2015, 11, 3536–3541.
- 18 A. Clarke, A. M. Howe, J. Mitchell, J. Staniland and L. A. Hawkes, *SPE J.*, 2016, **21**, 0675–0687.
- 19 J. D. Jacob, R. Krishnamoorti and J. C. Conrad, *Phys. Rev. E*, 2017, **96**, 1–13.
- 20 F. Babayekhorasani, D. E. Dunstan, R. Krishnamoorti and J. C. Conrad, *Soft Matter*, 2016, **12**, 5676–5683.
- 21 S. Aramideh, P. P. Vlachos and A. M. Ardekani, *J. Non-Newtonian Fluid Mech.*, 2019, 268, 75–80.
- 22 C. A. Browne, A. Shih and S. S. Datta, *Small*, 2020, **16**, 1903944.
- 23 J. Bear, Dynamics of Fluids in Porous Media, Dover, 1988.
- 24 M. Kumar and A. M. Ardekani, *Phys. Fluids*, 2021, 33, 074107.
- 25 M. Kumar and A. M. Ardekani, Eur. Phys. J.: Spec. Top., 2023, 232, 837–848.
- 26 M. Kumar and A. M. Ardekani, *Phys. Rev. Fluids*, 2022, 7, 093302.
- 27 M. Kumar, S. Aramideh, C. A. Browne, S. S. Datta and A. M. Ardekani, *Phys. Rev. Fluids*, 2021, **6**, 033304.
- 28 S. Kenney, K. Poper, G. Chapagain and G. F. Christopher, *Rheol. Acta*, 2013, **52**, 485–497.
- 29 M. Grilli, A. Vázquez-Quesada and M. Ellero, *Phys. Rev. Lett.*, 2013, **110**, 174501.
- 30 A. M. Howe, A. Clarke and D. Giernalczyk, *Soft Matter*, 2015, 11, 6419–6431.
- 31 X. Shi and G. F. Christopher, Phys. Fluids, 2016, 28, 124102.
- 32 A. Varshney and V. Steinberg, *Phys. Rev. Fluids*, 2017, 2, 051301.
- 33 B. Qin and P. E. Arratia, Phys. Rev. Fluids, 2017, 2, 083302.
- 34 D. M. Walkama, N. Waisbord and J. S. Guasto, *Phys. Rev. Lett.*, 2020, **124**, 164501.
- 35 C. A. Browne and S. S. Datta, Sci. Adv., 2021, 7, eabj2619.
- 36 S. J. Haward, C. C. Hopkins and A. Q. Shen, *Proc. Natl. Acad. Sci. U. S. A.*, 2021, **118**, e2111651118.
- 37 D. Kawale, E. Marques, P. L. J. Zitha, M. T. Kreutzer, W. R. Rossen and P. E. Boukany, *Soft Matter*, 2017, 13, 765–775.
- 38 S. De, J. van der Schaaf, N. G. Deen, J. A. Kuipers, E. A. Peters and J. T. Padding, *Phys. Fluids*, 2017, **29**, 113102.
- 39 M. Kumar, J. S. Guasto and A. M. Ardekani, *Proc. Natl. Acad. Sci. U. S. A.*, 2023, **120**, e2211347120.
- 40 C. Faustino, A. F. Bettencourt, A. Alfaia and L. Pinheiro, J. Chem. Educ., 2015, 92, 936–939.

- 41 S. L. Anna and G. H. McKinley, J. Rheol., 2001, 45, 115-138.
- 42 J. P. Rothstein and G. H. McKinley, *J. Non-Newton. Fluid Mech.*, 1999, **86**, 61–88.
- 43 J. P. Rothstein and G. H. McKinley, *J. Non-Newton. Fluid Mech.*, 2001, **98**, 33–63.
- 44 R. Bird, R. Bird, R. Armstrong and O. Hassager, Dynamics of Polymeric Liquids, *Fluid Mechanics*, Wiley, 1987, vol. 1.
- 45 W. Thielicke and E. J. Stamhuis, *J. Open Res. Softw.*, 2014, 2, e30.
- 46 R. B. Bird, C. F. Curtiss, R. C. Armstrong and O. Hassager, Dynamics of polymeric liquids, *Kinetic theory*, John Wiley and Sons Inc., New York, NY, United States, 2nd edn, 1987, vol. 2.
- 47 R. B. Bird, P. J. Dotson and N. L. Johnson, J. Non-Newtonian Fluid Mech., 1980, 7, 213–235.
- 48 B. Purnode and M. J. Crochet, J. Non-Newtonian Fluid Mech., 1998, 77, 1–20.
- 49 M. D. Chilcott and J. M. Rallison, J. Non-Newtonian Fluid Mech., 1988, 29, 381–432.
- 50 P. J. Oliveira, Acta Mech., 2002, 158, 157-167.
- 51 F. Pimenta and M. A. Alves, *J. Non-Newtonian Fluid Mech.*, 2017, 239, 85-104.
- 52 H. Jasak, A. Jemcov and Z. Tukovic, *International Workshop on Coupled Methods in Numerical Dynamics*, 2007, pp.1–20.
- 53 R. Fattal and R. Kupferman, *J. Non-Newtonian Fluid Mech.*, 2004, **123**, 281–285.
- 54 M. E. Rosti, F. Picano and L. Brandt, in *Numerical Approaches to Complex Fluids*, ed. F. Toschi and M. Sega, Springer International Publishing, Cham, 2019, pp.1–34.
- 55 J. L. Favero, A. R. Secchi, N. S. Cardozo and H. Jasak, *J. Non-Newtonian Fluid Mech.*, 2010, **165**, 1625–1636.
- 56 G. H. McKinley, *Transp. Processes Bubbles, Drops, Part.*, 2001, 338–375.
- 57 C. Wagner, Y. Amarouchene, D. Bonn and J. Eggers, *Phys. Rev. Lett.*, 2005, **95**, 164504.

- 58 M. Verhoef, B. van den Brule and M. Hulsen, *J. Non-Newtonian Fluid Mech.*, 1999, **80**, 155–182.
- 59 G. Haller, Annu. Rev. Fluid Mech., 2015, 47, 137-162.
- 60 G. A. Voth, G. Haller and J. P. Gollub, *Phys. Rev. Lett.*, 2002, 88, 254501.
- 61 S. Parsa, J. S. Guasto, M. Kishore, N. T. Ouellette, J. P. Gollub and G. A. Voth, *Phys. Fluids*, 2011, 23, 043302.
- 62 A. Dehkharghani, N. Waisbord, J. Dunkel and J. S. Guasto, *Proc. Natl. Acad. Sci. U. S. A.*, 2019, **116**, 11119–11124.
- 63 N. Stoop, N. Waisbord, V. Kantsler, V. Heinonen, J. S. Guasto and J. Dunkel, *J. Non-Newtonian Fluid Mech.*, 2019, **268**, 66–74.
- 64 G. I. Taylor, Proc. R. Soc. London, Ser. A, 1953, 219, 186–203.
- 65 R. Aris and G. I. Taylor, Proc. R. Soc. London, Ser. A, 1956, 235, 67–77.
- 66 T. Perkins and O. Johnston, Soc. Pet. Eng. J., 1963, 3, 70-84.
- 67 R. S. Maier, D. M. Kroll, R. S. Bernard, S. E. Howington, J. F. Peters and H. T. Davis, *Phys. Fluids*, 2000, 12, 2065–2079.
- 68 G. Taylor, Proc. R. Soc. A, 1951, 209, 447-461.
- 69 D. E. Smith, H. P. Babcock and S. Chu, *Science*, 1999, 283, 1724–1727.
- 70 D. Kawale, G. Bouwman, S. Sachdev, P. L. J. Zitha, M. T. Kreutzer, W. R. Rossen and P. E. Boukany, *Soft Matter*, 2017, 18, 8745–9755.
- 71 O. Mokhtari, J.-C. Latché, M. Quintard and Y. Davit, *J. Fluid Mech.*, 2022, **948**, A2.
- 72 C. Li Sun and H. Y. Huang, Biomicrofluidics, 2016, 10, 1-13.
- 73 S. J. Haward, K. Toda-Peters and A. Q. Shen, *J. Non-Newtonian Fluid Mech.*, 2018, 254, 23–35.
- 74 D. W. Carlson, K. Toda-Peters, A. Q. Shen and S. J. Haward, J. Fluid Mech., 2022, 950, A36.
- 75 D. Roote, Ground Water Remediation Technology Analysis Center (available at https://www.gwrtac.org), 1998.